Journal of Power Sources 208 (2012) 296–305

Contents lists available at SciVerse ScienceDirect

Journal of Power Sources

journal homepage: www.elsevier.com/locate/jpowsour

Calendar aging of a graphite/$LiFePO_4$ cell

M. Kassem[a,*], J. Bernard[b], R. Revel[b], S. Pélissier[c], F. Duclaud[d], C. Delacourt[a,*]

[a] Laboratoire de Réactivité et Chimie des Solides, UMR CNRS 6007, Université de Picardie Jules Verne, 80039 Amiens, France
[b] IFP Energies Nouvelles, Rond-point de l'échangeur de Solaize, BP 3, 69360 Solaize, France
[c] Laboratoire Transports et Environnement, Institut Français des Sciences et Technologies des Transports, de l'Aménagement et des Réseaux, 69675 Bron, France
[d] Laboratoire d'Essais et d'Expérimentations Electrique, EIGSI La Rochelle, 17041 La Rochelle, France

ARTICLE INFO

Article history:
Received 23 January 2012
Received in revised form 16 February 2012
Accepted 17 February 2012
Available online 25 February 2012

Keywords:
Graphite/LFP cells
Storage
Capacity fade
Impedance
Rate capability
PITT

ABSTRACT

Graphite/LFP commercial cells are stored under 3 different conditions of temperature (30 °C, 45 °C, and 60 °C) and SOC (30%, 65%, and 100%) during up to 8 months. Several non-destructive electrochemical tests are performed at different storage times in order to understand calendar aging phenomena. After storage, all the cells except those stored at 30 °C exhibited capacity fade. The extent of capacity fade strongly increases with storage temperature and to a lesser extent with the state of charge. From in-depth data analysis, cyclable lithium loss was identified as the main source of capacity fade. This loss arises from side reactions taking place at the anode, e.g. solvent decomposition leading to the growth of the solid electrolyte interphase. However, the existence of reversible capacity loss also suggests the presence of side reactions occurring at the cathode, which are less prominent than those at the anode. The analyses do not show any evidence about active-material loss in the electrodes. The cells do not suffer substantial change in internal resistance. According to EIS analysis, the overall impedance increase is 70% or less.

1. Introduction

Lithium-ion batteries are now the dominant rechargeable systems in the market. They have attracted a great deal of interest due to their high energy and power densities. They are widely used in portable electronics (e.g., cellular phones, digital cameras, and laptop computers) and are considered as the perfect candidates for electric transportation (e.g., electric vehicles (EVs) and hybrid electric vehicles (HEVs)). As most of the battery systems, Li-ion batteries suffer capacity and power fade during both cycling and storage. Although aging is not much an issue for portable electronic devices, it becomes absolutely crucial for EVs and HEVs application where substantially longer lifetime is requested. The cycle life performance of lithium-ion batteries was studied extensively and is well-documented in the literature. It was found that the performance loss is caused by various mechanisms, which depend on the electrode materials and on the adopted usage protocol [1–11]. This loss can be attributed to several processes such as (i) the (primary) loss of cyclable lithium which is related to the side reactions occurring at both electrodes (e.g., SEI growth at carbon anode due to electrolyte decomposition) and leading to an increase of the cell imbalance, (ii) the (secondary) loss of active materials (e.g., material dissolution, structural degradation, particle isolation, and electrode delamination), and (iii) impedance increase of the cell (e.g., passive films at the active particle surface and loss of electrical contact within the porous electrode). In addition to cycling performance, another crucial factor for lithium-ion battery applications is the storage performance. The calendar life of these batteries represents an important factor in the evaluation of their dependability and stability and the corresponding tests are designed to evaluate the cell degradation as a result of passage of time with minimal usage. A personal EV spends about 95% of its time in parking mode, hence the relevance of studying calendar aging. Several calendar life performance studies exist in the literature [12–22]. Broussely et al. [12] reported the loss of cyclable lithium due to side reactions at the graphite negative electrode as the main source of aging during storage at high temperature. Increase of cell impedance with storage time was reported in Refs. [14,16,18]. Zhang and White [22] have performed a calendar life study on Li-ion pouch cells and observed that the capacity fade is linear with time at low temperature and nonlinear at high temperature and that the anode experienced a severe loss of active carbon during storage at high temperature (60% loss at 25 °C, and over 80% loss at 35 °C and 45 °C).

We are particularly interested with the performance decay because of aging processes in LFP-based cells. These cells have undergone a formidable development qualifying them to meet the demands of high-rate devices (e.g., HEV) and to compete with

* Corresponding authors. Tel.: +33 3 22 82 75 89; fax: +33 3 22 82 75 90.
E-mail addresses: mohammad.kassem@u-picardie.fr (M. Kassem), charles.delacourt@u-picardie.fr (C. Delacourt).

0378-7753/$ – see front matter © 2012 Elsevier B.V. All rights reserved.
doi:10.1016/j.jpowsour.2012.02.068

cells based on other cathode materials, such as layered and spinel oxides. The olivine LFP cathode, reported for the first time by Padhi et al. [23,24], has a theoretical capacity of 170 mAh g^{-1} and a redox potential around 3.43 V vs. Li electrode [25]. It is safe, because of a high thermal stability, and has a low toxicity and a low cost compared to cathodes such as $LiCoO_2$. Several aging studies concerned with life performance of LFP-based cells are found in the literature [26–38]. Refs. [26–28] reported that the major cause of capacity fade arises from side reactions that consume cyclable lithium and increases the interfacial resistance of the anode. Dubarry and Liaw [29] combined the differential-capacity analysis and SOC tracing of the cell at 600 cycles and concluded that aging mainly results from the formation of a Li-consuming SEI layer at the graphite electrode. Some authors suggested that the cathode is the main contributor to capacity fade. Amine et al. [30] and Koltypin et al. [31,32] confirmed iron dissolution from LFP electrodes and attributed the capacity fade to the formation of interfacial films produced on the graphite electrodes as a result of possible catalytic effects of the metallic iron particles. Liu et al. [33] analyzed the differential curves that revealed loss of cyclable lithium as well as degradation of the carbon anode. Dubarry et al. [35] reported that the cells suffer severe degradation at 60 °C that could be explained by electrochemical milling of grains. This effect might cause some loss of active material in the positive electrode and consequently induce a loss of Li inventory, due to SEI formation on the fresh surface created, especially at elevated temperatures. Safari and Delacourt [37], in their aging study of LFP/C cells, identified the depletion of cyclable lithium and the partial loss of graphite active-material particles as the two contributors to the capacity decline. However, the post mortem analysis [38] revealed that the graphite active-material loss is not present for cells under storage conditions and is only experienced for the cells under cycling. The aim of the present work is to study the effect of open-circuit-potential storage on the performance of commercial graphite/LFP cells. In this study, aging results under storage are presented and the effect of storage temperature and storage state of charge (SOC) on aging is discussed thoroughly.

2. Experimental

Experimental studies were performed on graphite/$LiFePO_4$ cells (LiFeBatt™ X1P, 8 Ah, 38123 [39]) designed for power-type applications. These cells consist of C–$LiFePO_4$ cathode and graphite anode with a nominal capacity of 8 Ah and cell dimensions of 123 mm long, 38 mm diameter and a weight of 290 g. The cells were stored at 3 different temperatures: 30 °C, 45 °C, and 60 °C and at 3 different states of charge (SOC_{nom}): 30%, 65%, and 100%. This means that there are a total of 9 different storage conditions. For each storage condition, 3 cells were aged. Thus, the total number of cells tested during this aging study amounts to 27. All the experiments were conducted using a multipotentiostat (VMP3, Biologic, France) outfitted with a 10 A or 20 A booster, except the rate–capability tests for which a multichannel battery tester (SBT2050, PEC, Belgium) was used. The aging tests were performed in a temperature-controlled environment. Climatic chambers (Binder KB53, Memmert ULE 800, or Friocell 700) were used for this purpose.

Before performing the initial checkup of the cells, they were preconditioned using six charge/discharge cycles. This step allowed removing possible outliers. Discharge/charge cycles consisted of a constant current discharge at 1 C_{nom} down to 2 V, followed by 30 min rest, a constant current constant voltage (CCCV) charge [i.e., 1 C_{nom} (8 A) up to 3.65 V and potential hold at 3.65 V until a cut-off current $|I| = C_{nom}/20$], and another 30 min rest period.

After this preconditioning step, a checkup procedure was carried out. It included a capacity measurement followed by electrochemical impedance spectroscopy (EIS) at different SOCs. The capacity measurement was done using the exact same discharge/charge procedure as that described above for cell preconditioning. Two discharge/charge cycles were performed in order to extract reversible and irreversible capacity losses (see Section 3.5). The EIS measurement was carried out in the frequency range of 10 kHz to 10 mHz with a 5 mV RMS sinusoidal potential. The impedance spectra were measured at different nominal checkup SOCs ($SOC_{nom,ck}$ = 100%, 80%, 60%, 40%, and 20%). These nominal SOCs were set from a fully charged state (the cells are at SOC = 100% after the 2 cycles) by using a 1 C_{nom} discharge rate during 12 min, 24 min, 36 min, and 48 min in order to set the $SOC_{nom,ck}$ 80%, 60%, 40%, and 20%, respectively. After the checkup, open-circuit-potential storage was resumed after the cells were reset to their storage SOC_{nom} (100%, 65%, or 30%) and temperature (30 °C, 45 °C, or 60 °C). To reset the SOC, a 1 C_{nom} discharge rate was applied to the fully charged cells during either 21 min or 42 min for SOC_{nom} 65% and 30%, respectively. To evaluate the state of health (SOH) of the cells during storage, intermediate checkups were performed during an interval of several months. The storage was interrupted, the cell temperature was set to 25 °C, and the cell capacity and EIS were measured. The protocol carried out during these intermediate checkups is identical to that performed for initial checkup. At the end of the aging period, an extra checkup was performed. It included potentiostatic intermittent titration technique (PITT) and a rate capability test. The low-rate PITT test was performed on 10 graphite/LFP cells (a fresh cell and nine aged cells) and consisted of a staircase potential profile during which the cell potential was increased (decreased) by 5 mV increments between 2 V and 3.65 V and the current decay vs. time was measured at each potential step. Each individual titration is terminated when the absolute current reached a value of $C_{nom}/20$. The rate–capability tests were performed on the same ten batteries, using the multichannel battery tester (SBT2050, PEC, Belgium) at C-rates between $C_{nom}/25$ and 5 C_{nom} with a voltage window of 2.0–3.65 V. A CCCV protocol was used for both charge and discharge modes (CV until $|I| < C_{nom}/50$), and there was a 1 h rest period between consecutive charge (discharge) and discharge (charge). The surface temperature of the different cells was recorded using a K-type thermocouple.

3. Results and discussion

3.1. Capacity fade

Fig. 1 shows the charge and discharge profiles of 3 different cells at different storage periods at a fully charged state (SOC_{nom} 100%) and at temperatures (a) 30 °C, (b) 45 °C, and (c) 60 °C. Before storage, the fresh cells show slightly different initial discharge capacities. The average 1 C discharge capacity for all 27 cells before storage is $Q_{1C} = 8.517 \pm 0.043$ Ah. Cell specifications indicate a nominal capacity $Q_{nom} = 8.0$ Ah, which is less than the average 1 C discharge capacity we measured. The dispersion in 1 C discharge capacity values reflects some dispersion in the manufacturing process. Upon storage, the cells stored at 45 °C and 60 °C undergoes capacity fade, which is larger for the cell stored at 60 °C. For the cell stored at 30 °C, however, a slight increase in capacity is observed upon storage. This increase in capacity is discussed later on in the manuscript. The discharge capacities of all 27 cells, measured at 1 C_{nom} rate during the intermediate checkups at 25 °C, are represented in Fig. 2. Three cells in each case of the nine different storage conditions are tested for a maximum period of 8 months and different behaviors depending on storage temperature and SOC are observed. The initial spread in capacity values mentioned above for the fresh cells is confirmed. It is small for the cells to be stored at 45 °C and 60 °C

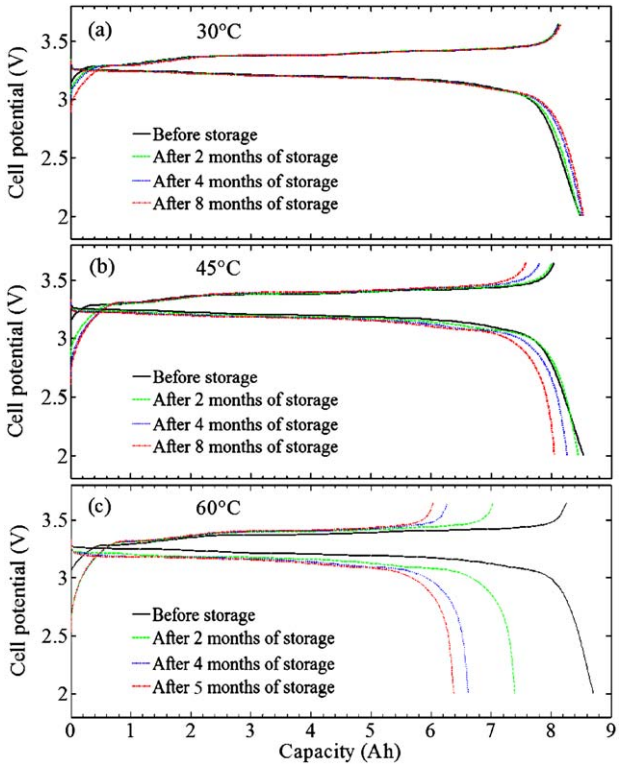

Fig. 1. Charge/discharge profiles measured at 1 C_{nom} and 25 °C for cells under storage at SOC_{nom} = 100% and at temperature (a) 30 °C, (b) 45 °C, and (c) 60 °C.

(Fig. 2(b) and (c)); however, it is surprisingly large for those to be stored at 30 °C (Fig. 2(a)), which is fortuitous. For the cells aged under the most severe aging conditions (e.g., 60 °C, SOC_{nom} 65% or 100%), there is more dispersion in capacity compared to that at initial time, suggesting an additional dispersion due to aging.

Fig. 2(a) shows that, after 240 days (8 months) of storage, the capacity increased by 1.8%, 1.07%, and 1% for SOC_{nom} 30%, 65%, and 100%, respectively. Meanwhile, Fig. 2(b) and (c) shows that

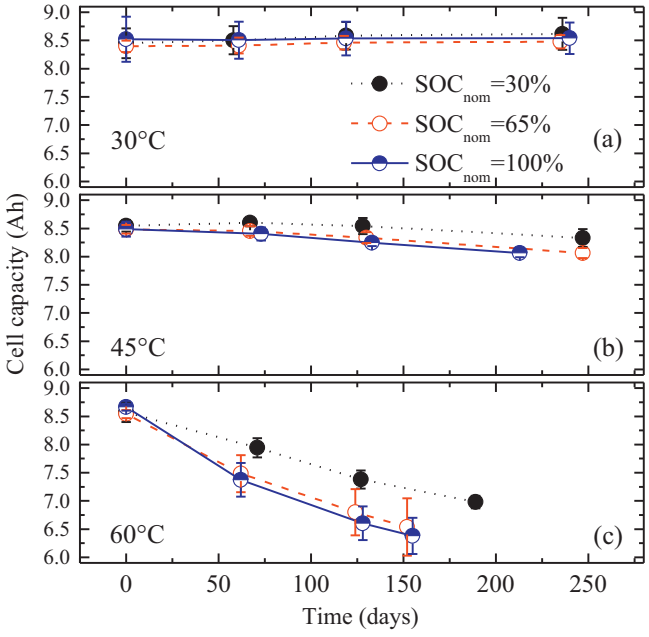

Fig. 2. Discharge capacities measured at 1 C_{nom} and 25 °C for the 27 cells under different storage conditions of temperature and SOC.

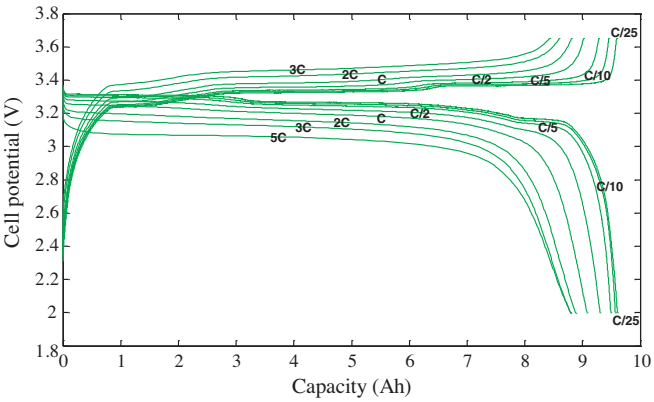

Fig. 3. Galvanostatic charge/discharge potential profiles measured at various C-rates and 25 °C for the fresh cell.

the capacity fade is fairly linear as a function of storage time and at a specified temperature, more capacity fade is experienced at higher storage SOC. At 45 °C, after nearly 214–247 days of storage, the capacity has decreased by 2.1%, 4.9%, and 5.7% for SOC_{nom} 30%, 65%, and 100%, respectively. This decrease becomes much more substantial for the cells stored at 60 °C for which the capacity fade percentages of the cells (~155–188 days of aging) are about 18.1%, 23.7%, and 26.9% for SOC_{nom} 30%, 65% and 100%, respectively.

3.2. Rate–capability test

An example of charge/discharge potential profiles at various C-rates ranging from C_{nom}/25 to 3 C_{nom} during charge and from C_{nom}/25 to 5 C_{nom} during discharge is presented in Fig. 3 for the fresh cell at 25 °C. The charge/discharge rate–capability curves of the cell can be derived from this type of measurement and are provided in Fig. 4 for the fresh cell and for the aged cells at the end of the aging tests. When the cell impedance increases, cut-off potentials are reached sooner for a given cell and there is a decline in the rate capability of the cell. So, any change in the current dependence of the polarization effects in the cell is expected to show up as a change in the slope of the rate–capability curves of Fig. 4. During charge, the rate capability is retained for all aging conditions (Fig. 4(a)–(d)). The rate–capability curves only translate along the capacity axis, especially for the cells stored at 60 °C, in agreement with the capacity loss reported above. However, there is virtually no change in the rate capability, which suggests negligible or minor increase of the cell resistance upon storage. During discharge, the rate capability curve clearly levels off at high C-rate (Fig. 4(e)), which probably results from a thermal effect (the surface temperature of the cell is 44 °C at 5 C_{nom}). Beside the same translation effect previously observed for the rate capability on charge, there is an overall improvement in the rate capability on discharge especially for the cells aged under the most severe storage conditions (high temperature and SOC). To understand these trends in rate capability, one must recall first that this type of battery (graphite/LFP) is limited on charge by Li removal from the LFP cathode and on discharge by Li intercalation into the graphite anode [40]. Hereby, the retention of rate capability for both fresh and aged cells on charge suggests the absence of a remarkable deterioration of the LFP electrode. On the other hand, the gradual improvement in rate capability on discharge might be explained by a substantial loss of cyclable lithium, which restricts the operating stoichiometry window of LFP to a lower maximum lithium stoichiometry, where the rate capability of the electrode is larger [29,37,38]. Some insights about the existence of cyclable lithium losses are provided later on in the manuscript (Section 3.4). The cells stored at 30 °C (Fig. 4(f)) deserve further attention. They undergo a slight decrease

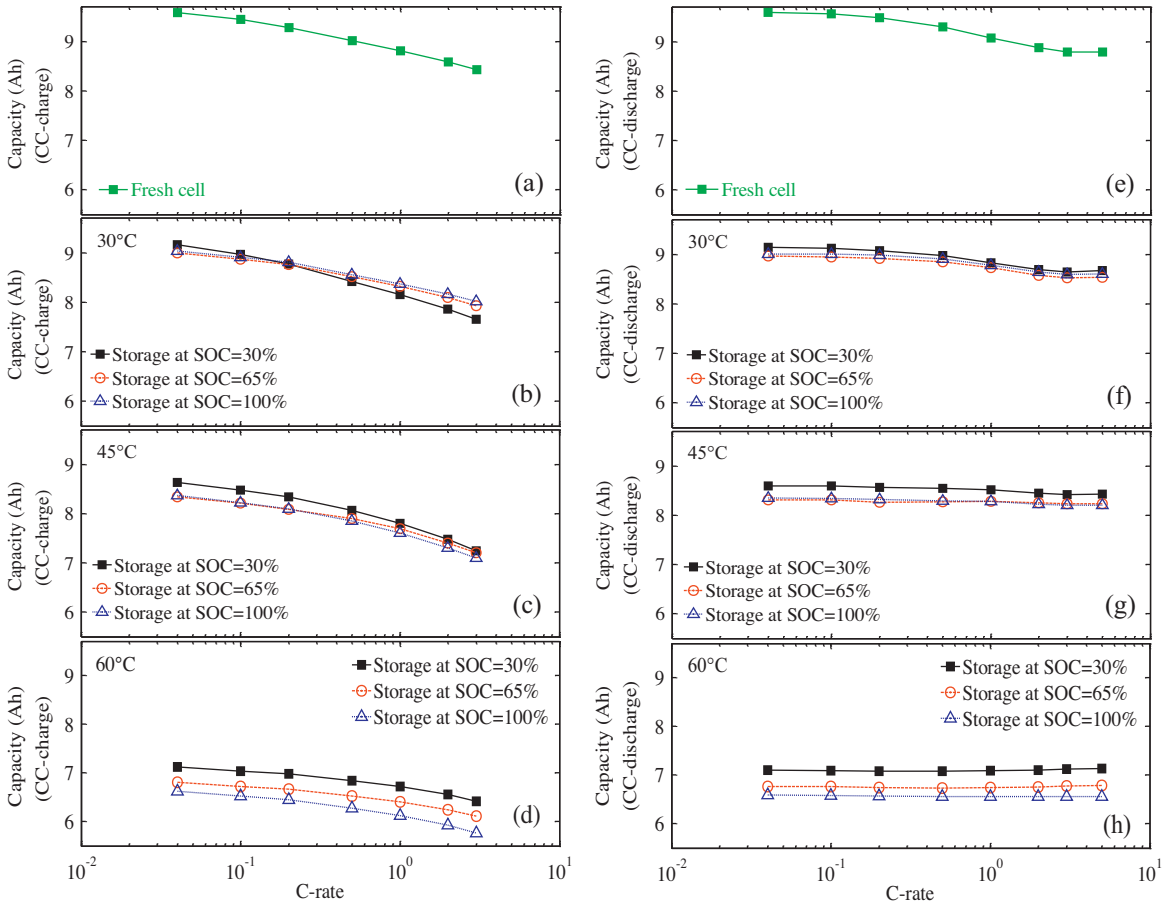

Fig. 4. Rate capability of both fresh and aged cells under different storage conditions of temperature and nominal SOCs, measured at 25 °C at the end of aging test. (a)–(d) Rate capability on charge; (e)–(h) rate capability on discharge.

in (low-rate) capacity when compared to the fresh cell (Fig. 4(e)) and show an improvement in rate capability. This result differs from the increase of 1 C_{nom} capacity reported in Fig. 2(a) for the cells stored at 30 °C, which probably arises from the improvement of discharge rate capability that compensates for the slight (low-rate) capacity loss outlined in Fig. 4(f).

3.3. Impedance test

From EIS spectra, it is possible to gain insight into the origin of the impedance increase because the various phenomena are separated according to their time constant. The main limitation is that it is difficult to decipher the contributions of each electrode to the overall impedance increase. EIS measurement on separate electrodes (once the cell is taken apart or by using a reference electrode) is necessary to this end. Fig. 5 shows a typical impedance spectrum of a fresh graphite/LFP cell at 25 °C and at various $SOC_{nom,ck}$ (20%, 40%, 60%, 80%, and 100%). The spectrum in Nyquist representation is characterized by an inductive part at frequencies higher than 270 Hz, a semicircle between 270 Hz and 13 Hz and a nearly linear tail at lower frequency. Different impedance contributions are labeled in Fig. 5. We define (a) R_{hf} as the high-frequency intercept with the real axis that is related to the electrolyte resistance and the resistance of external leads and connections, (b) R_{sc} as the semi-circle resistance at medium frequency featuring charge-transfer kinetics and other interfacial contributions like passivating films, (c) R_t as the tail resistance at low frequency featuring transport limitations in solid and liquid phases, and (d) R_{tot} as the total

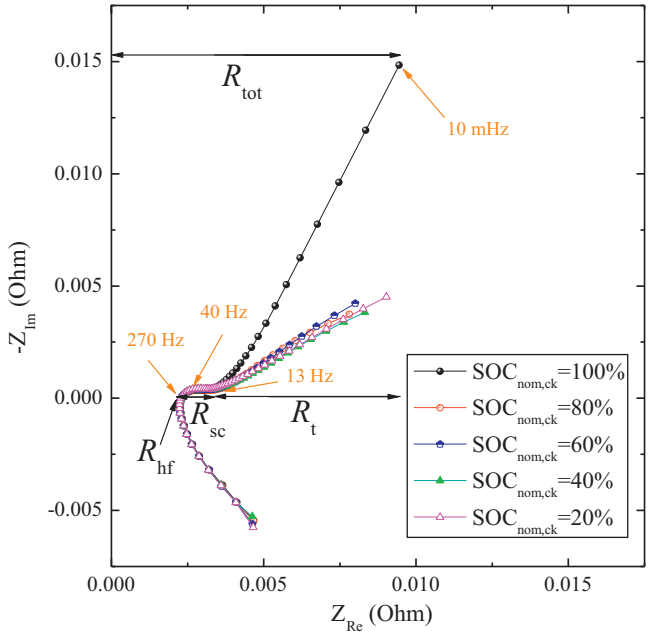

Fig. 5. Impedance spectra of the fresh cell measured at 25 °C and at different nominal checkup SOCs (20%, 40%, 60%, 80%, and 100%).

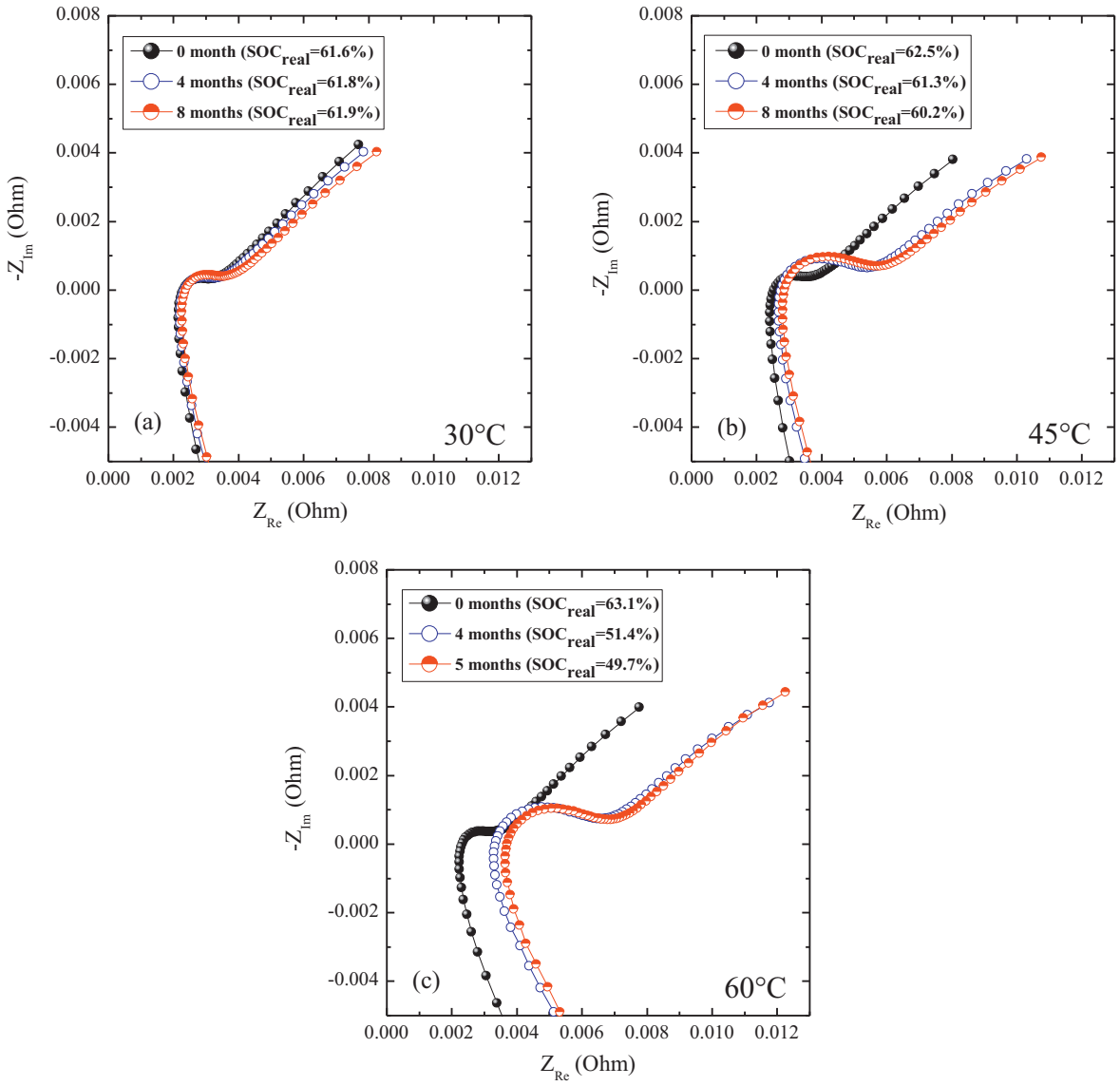

Fig. 6. Impedance spectra measured at 25 °C and $SOC_{nom,ck}$ = 60% for (a) a cell aged at 30 °C and SOC_{nom} = 100%, (b) a cell aged at 45 °C and SOC_{nom} = 100%, (c) a cell aged at 60 °C and SOC_{nom} = 100%. The real SOC values corresponding to each spectrum are provided in the plot legends.

resistance of the abovementioned three contributions ($R_{hf} + R_{sc} + R_t$). Fig. 5 shows that there is a little change of the overall impedance with the SOC at which it is measured, except for the extreme value ($SOC_{nom,ck}$ = 100%) for which the low frequency impedance is larger.

For the sake of comparison, the impedance spectra measured at 25 °C and $SOC_{nom,ck}$ = 60% of 3 cells aged at SOC_{nom} = 100% and 30 °C, 45 °C, or 60 °C are displayed in Fig. 6. The actual SOC specific to each spectrum is recalculated and provided in the legend of Fig. 6. Actual SOCs are quite close to the nominal ones for the cells aged at 30 °C and 45 °C, but are substantially lower for those aged at 60 °C, e.g., 13% less for the cell aged under the most severe aging condition (T = 60 °C and SOC_{nom} = 100%). Keeping in mind that the SOC influence is of minor impact (Fig. 5), comparing impedance spectra at different storage temperatures and SOCs is fairly reasonable. Fig. 6 shows a clear change of the spectra over aging time. The relative evolutions of R_{tot}, R_{hf}, R_{sc}, and R_t at $SOC_{nom,ck}$ = 60% are derived from the Nyquist plots and are represented in Fig. 7 as a function of aging time for all aging conditions. Two main features are observed, namely (i) the overall cell impedance strongly depends on storage temperature (total resistance values increase as storage temperature increase) and (ii) no clear influence of the storage SOC is observed. The impedance of the semicircle R_{sc} is the one that increases the most among all 3 different contributions during storage (Fig. 7(k) shows a maximum increase of about 300% after 5 months of storage at 60 °C), followed by the high-frequency resistance R_{hf} (60% maximum increase at 60 °C is shown in Fig. 7(j)) and by the low-frequency-tail resistance R_t (Fig. 7(l) presents a 25% maximum increase at 60 °C).

Considering that the overall impedance increase is about 70% max, the moderate increase of R_t suggests that bulk transport properties are almost unchanged over aging (absence of structural degradation). This result is in good agreement with the retention of rate capability during aging. The large increase of R_{sc} is related to either the presence of growing films at the particle surface like SEI at negative electrode but can also arise from electronic contact resistance that develops within the composite electrode [41], whereas the high-frequency resistance R_{hf} could result from a slight degradation of the electrolyte. Interestingly, Fig. 8 reveals a correlation between R_{hf} and R_{sc}, suggesting that electrolyte degradation and interfacial phenomena are linked with each other to some extent.

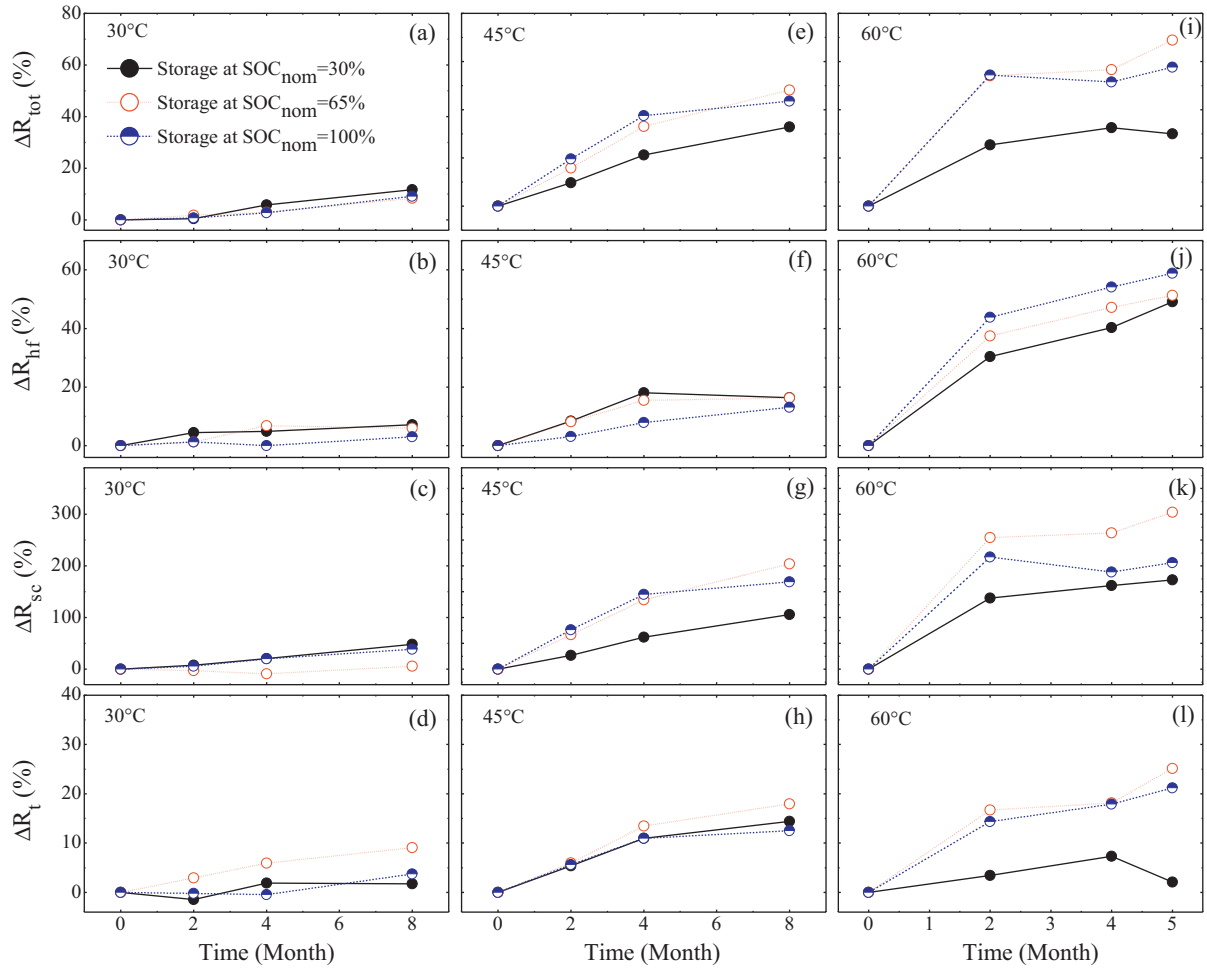

Fig. 7. Evolution of the total resistance R_{tot}, the ohmic resistance R_{hf}, the semicircle resistance R_{sc}, and the tail resistance R_t derived from the impedance spectra of the cells at 25 °C and $SOC_{nom,ck}$ = 60%.

3.4. PITT test

The charge/discharge voltage profiles of cells aged under nine different aging conditions are represented in Fig. 9 along with that of the fresh cell. There are four distinct groups distributed according to their storage temperature. The influence of storage temperature exceeds that of storage SOC, which is in complete agreement with the 1 C_{nom} capacity measurements reported in Fig. 2. Fig. 9 shows that, in comparison with the fresh cell, the group stored at 30 °C undergoes a capacity decrease by 5.0%, 6.3%, and 6.0% for SOC_{nom} 30%, 65%, and 100%, respectively. The group stored at 45 °C shows

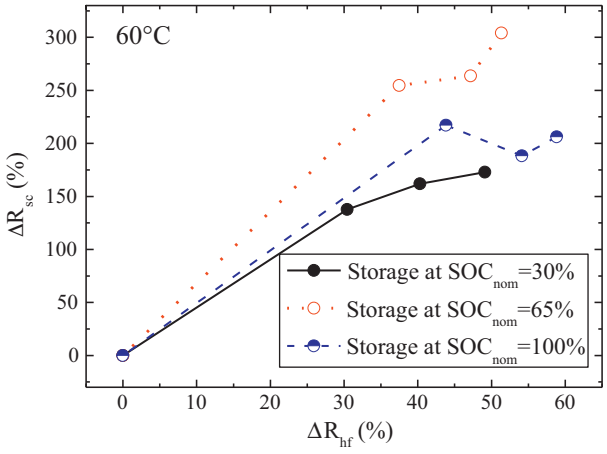

Fig. 8. Correlation plot of semicircle and high-frequency resistances for the cells aged at 60 °C and different nominal SOCs. The values were derived from the impedance spectra of the cells at 25 °C and $SOC_{nom,ck}$ = 60%.

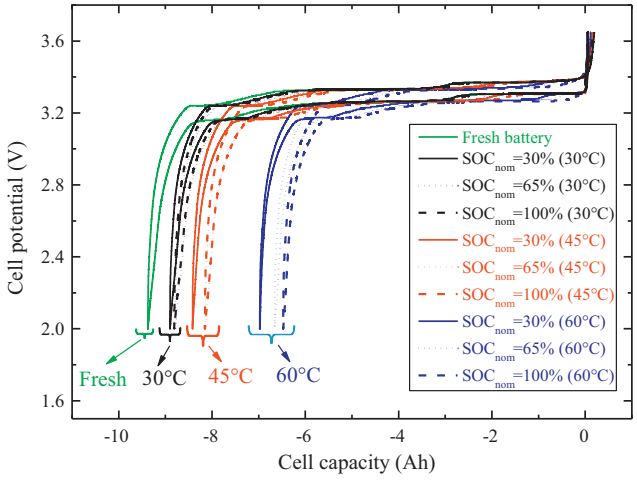

Fig. 9. Discharge/charge PITT between 3.65 V and 2.0 V at 25 °C for the fresh cell and for the cells aged under different storage conditions of temperature and SOC. The PITT measurement was performed at the end of aging test.

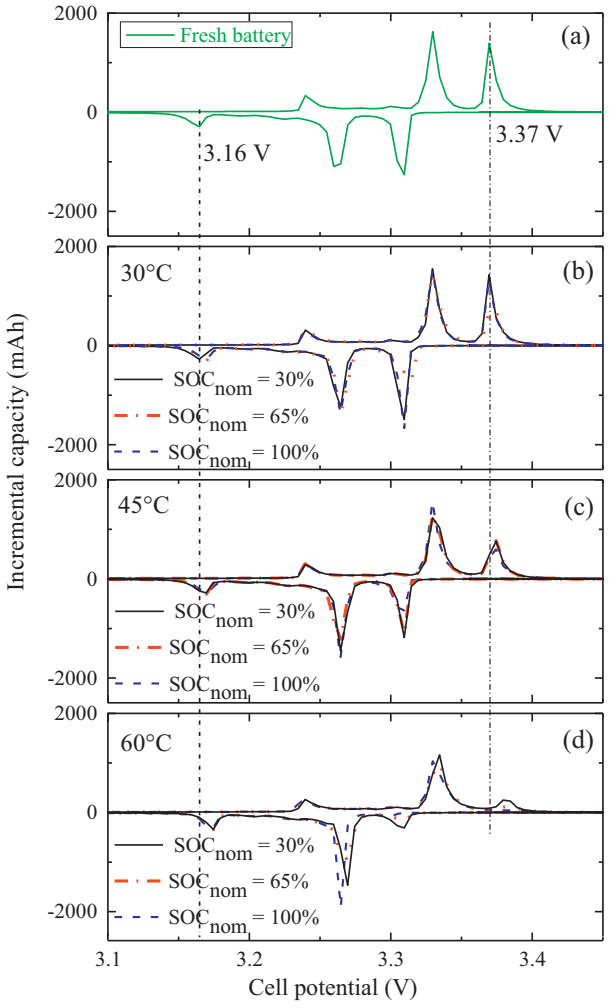

Fig. 10. Incremental capacity plot against cell potential derived from the PITT measurements at 25 °C that are reported in Fig. 9.

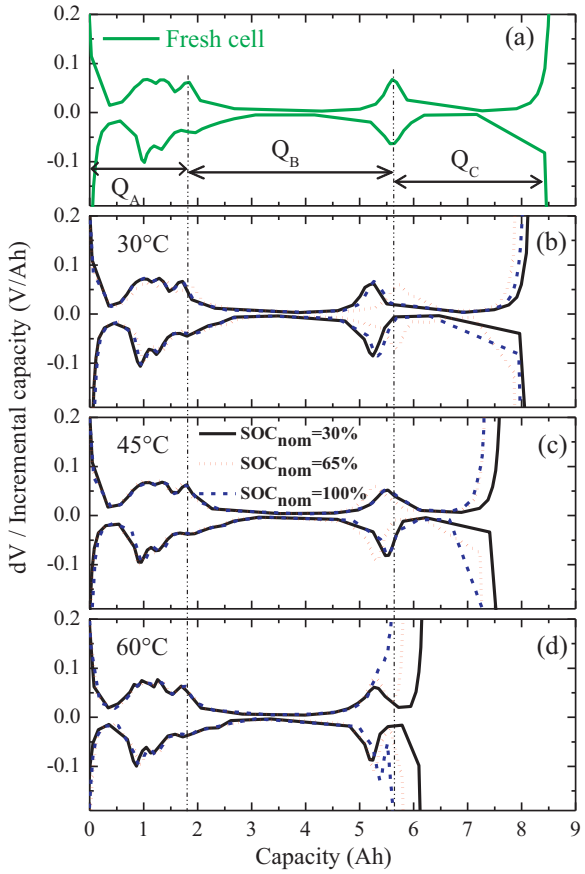

Fig. 11. Differential–voltage plot derived from the PITT measurements at 25 °C that are reported in Fig. 9.

a decrease of capacity by 10% for SOC_{nom} = 30% and by 13% for SOC_{nom} = 65% and 100%, and the last group stored at 60 °C undergoes a capacity decrease by 25%, 29%, and 31% for SOC_{nom} = 30%, 65%, and 100%, respectively.

Aside from the capacity, the shape of the voltage profile is interesting. There are three potential plateaus located at 3.24 V (3.16 V), 3.33 V (3.26 V), and 3.37 V (3.31 V) on charge (discharge). These three portions are the result of the difference between the potential plateau of the LFP cathode (3.43 V corresponding to Fe^{3+}/Fe^{2+} redox couple in LFP [23]) and the different potential stages of the graphite anode [29]. The flat portion at high cell potential shrinks progressively and ends up disappearing for the most severe storage condition (T = 60 °C and SOC_{nom} = 100%). This is clearly seen in Fig. 10, where the incremental capacity is plotted as a function of the cell potential. The 3 potential stages take the form of three prominent peaks (during either charge or discharge). Depending on storage conditions, two clear effects are distinguished from the incremental capacity curve, in comparison with the fresh cell: (i) a decrease of the peak area at high potential and (ii) a progressive shift of some peaks toward higher potential, such as the discharge peak at 3.16 V. The first effect suggests a change in the internal balancing of the cell, consistent with the loss of cyclable lithium due to side reactions at the anode. For the most severe condition, the high-potential peak completely vanishes (more cyclable lithium is consumed by the side reactions under this aging condition). The second effect, i.e., the peak shift, is also consistent with the loss of cyclable lithium, that yields a lower maximum lithium stoichiometry of the LFP electrode at the end of discharge, hence a higher potential of the electrode and thus of the cell. The postmortem analysis, performed on LFP and graphite electrodes recovered from these 10 commercial cells, shows a significant decrease of cyclable lithium content upon aging for some of the conditions. The detailed discussion of postmortem results will be reported elsewhere [40].

Another way to analyze the PITT data is to represent the inverse of incremental capacity as a function of capacity (Fig. 11). Similar information as in the case of a differential–voltage plot (i.e., Q–dV/dQ) can be derived from such a representation. It is useful to visualize the transitions between the different stages of the graphite electrode [42–44] and consequently to identify cyclable lithium loss as well as active material loss in a more quantitative manner.

In Fig. 11, the cell capacity is divided into 3 regions, namely regions A, B, and C. The capacity of region C decreases as the storage temperature increases, and even vanishes for the most severe storage condition (T = 60 °C and SOC_{nom} = 100%). The storage SOC is far less influential compared with storage temperature. Let us denote Q_A as the cell capacity in region A, Q_B as the cell capacity in region B, and Q_C as the cell capacity in region C. Q_A^0, Q_B^0, and Q_C^0 are the corresponding values for the fresh cell. These capacities are calculated from the distances between peaks in Fig. 11 and the relative evolution of the capacities in regions A, B, and C are represented in Fig. 12. The cell aged at 30 °C and SOC_{nom} = 65% might be an outlier because the corresponding capacity values are very far off. Q_C/Q_C^0 is quite sensitive to the temperature and clearly decreases when storage temperature increases. Meanwhile, Q_B/Q_B^0 and Q_A/Q_A^0 values remain nearly constant (regions A and B deliver

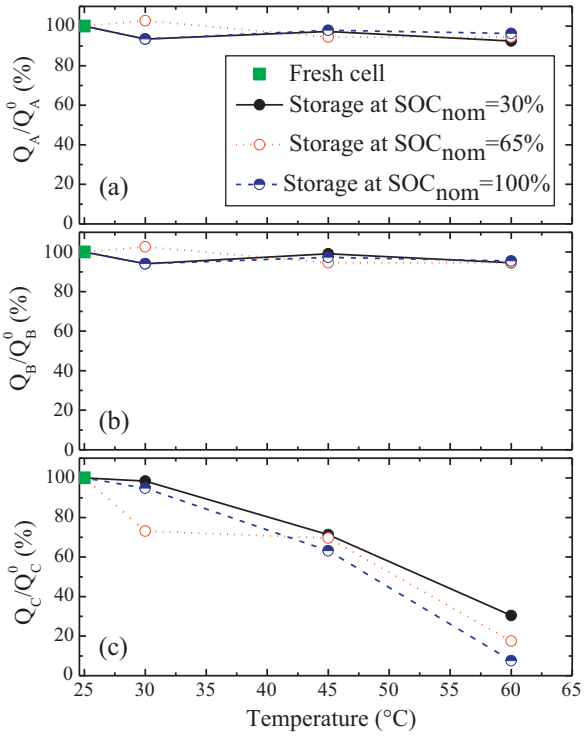

Fig. 12. Relative capacities in the 3 different regions, evaluated from the distances between peaks in Fig. 11.

about the same capacity as for the fresh cell). The loss of cyclable lithium is at the origin of this aging behavior. The gradual depletion of cyclable lithium shortens the operating stoichiometry window of the electrodes. Any other source of aging such as loss of active material at the negative electrode is not to be considered as outlined by the retention in the values of Q_B/Q_B^0 and Q_A/Q_A^0. It is difficult from the analysis, however, to rule out a partial loss of active material at the positive electrode. However, we anticipate that a partial loss of LFP would lower the rate capability of the cell on charge, where delithiation of LFP is limiting, which is not the case experimentally.

3.5. Reversible vs. irreversible capacity losses

Reversible and irreversible capacity losses of the OCP-stored cells were determined from the two discharge/charge cycles during the intermediate and final checkups (see Section 2). Let us denote the CCCV discharge capacity of the cell after storage $Q_{1,i}$ and $Q_{2,i}$ for the first and second discharges of the cell during characterization # i, respectively. With this notation, $Q_{2,i-1}$ stands for the second-discharge capacity of the cell at intermediate characterization # $i-1$. Reversible and irreversible capacity losses are calculated according to the following equations:

$$\Delta Q_{\mathrm{tot},i} = [Q_{2,i-1} - (1 - \mathrm{SOC_{nom}})Q_{\mathrm{nom}}] - Q_{1,i}$$

$$\Delta Q_{\mathrm{irr},i} = Q_{2,i-1} - Q_{2,i}$$

$$\Delta Q_{\mathrm{rev},i} = \Delta Q_{\mathrm{tot},i} - \Delta Q_{\mathrm{irr},i}$$

where $\Delta Q_{\mathrm{tot},i}$, $\Delta Q_{\mathrm{irr},i}$, and $\Delta Q_{\mathrm{rev},i}$ are namely the total, irreversible and reversible capacity losses arising from cell storage between two consecutive intermediate characterizations, respectively. Q_{nom} (8 Ah) stands for the nominal capacity.

Fig. 13 shows the 3 different types of capacity losses/gains calculated for the 27 cells under storage. For all the nine storage conditions, each type of capacity loss/gain is accumulated over the entire storage time and the influence of temperature and SOC on capacity loss/gain is qualitatively similar for the three cells aged under similar conditions. The cells aged at 45 °C or 60 °C experience both reversible and irreversible capacity losses. Whereas irreversible and reversible losses are very similar in magnitude at 45 °C, irreversible losses substantially exceed reversible ones at 60 °C. This point is discussed in more details in the following. The cells aged at 30 °C and $\mathrm{SOC_{nom}}$ = 30% or 65%, however, exhibit a total capacity "gain" that mostly results from the reversible part, i.e., the irreversible "gain" is small.

The previous tests showed that the irreversible capacity loss results solely from the loss of cyclable lithium. Structural

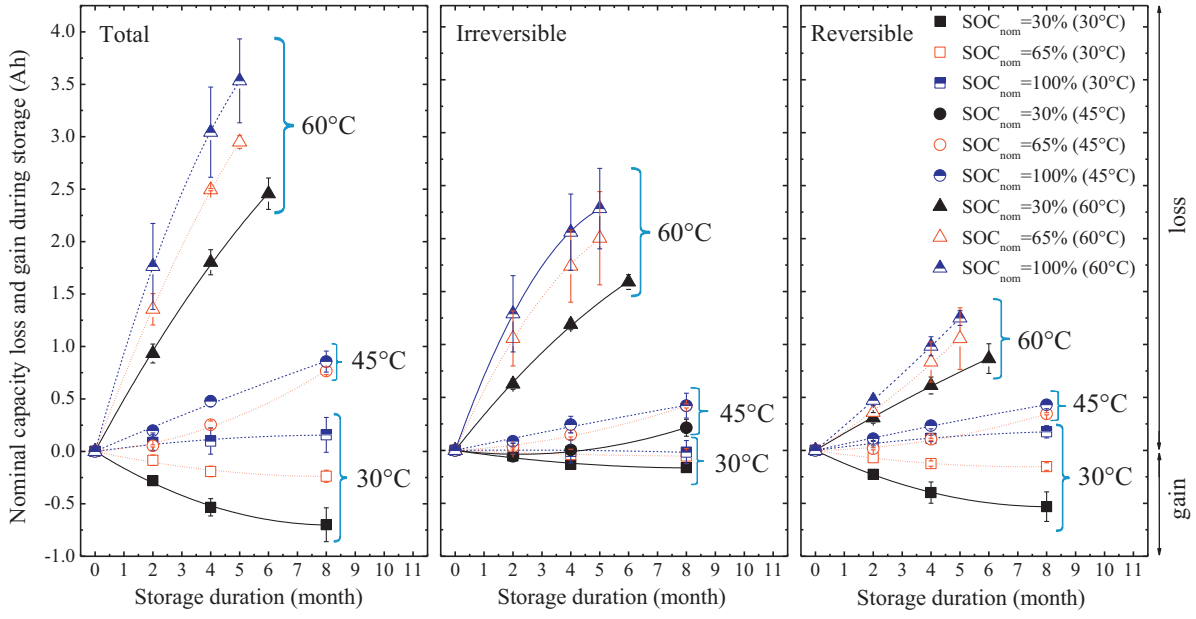

Fig. 13. Accumulated total, irreversible, and reversible capacity losses/gains of the cells during OCP storage at different temperatures and nominal SOCs. Losses are calculated from 1 C_{nom} capacity measurements during checkups at 25 °C. Reversible and total losses for the cell aged at 45 °C and $\mathrm{SOC_{nom}}$ = 65% are not represented in Fig. 13 due to a large dispersion between the 3 cells for this aging condition. The error bars correspond to the scatter for the three elements aged under similar aging conditions.

degradation and loss of active material at the electrodes are not observed and the postmortem analyses performed on the recovered individual electrodes confirm the above results [40]. The loss of cyclable lithium because of side reactions at the graphite electrode (e.g., the side reaction(s) at the interface between the electrode material and the electrolyte) was found to be responsible for a wide variety of aging phenomena in Li-ion batteries with carbonaceous anode [2,12]. Our impedance measurements confirm the existence of such side reactions at the electrode/electrolyte interface (correlation between electrolyte and interfacial resistance increase). Spotnitz [45] and Ozawa et al. [46] proposed that the oxidation of lithiated graphite negative electrode (low potential) and the reduction of delithiated positive electrode (high potential) by the electrolyte can lead to reversible and irreversible loss of cell capacity. A shuttle mechanism, in which the same species is reduced at one electrode (anode) and oxidized at another (cathode), can be at the origin of reversible capacity loss [47]. In this case, equal amount of cyclable lithium is exchanged between electrodes and electrolyte at both electrodes. The existence of both irreversible and reversible capacity losses suggests that the electrode/electrolyte interaction at the graphite electrode is not the only side reaction taking place in the cell. The reversible capacity loss is explained by the existence of side reactions at both electrodes and the non-zero irreversible capacity loss under storage suggests that the side reaction extent at the graphite electrode exceeds that at the positive electrode. Under this hypothesis, the charge consumed in the side reaction at the cathode corresponds to the reversible capacity loss (i.e., ΔQ_{rev}) whereas that at the anode corresponds to total capacity loss (i.e., $\Delta Q_{irr} + \Delta Q_{rev}$). Safari and Delacourt [37], based upon an analysis of the potential variations of graphite/LFP cells during OCP storage, demonstrated the contribution of both electrodes to the aging process under storage and that a minor lithium uptake due to side reaction at the charged LFP electrode partially compensates for the lithium release because of side reaction leading to SEI growth at the graphite electrode. In Fig. 13, we anticipate that the reversible and irreversible capacity losses originate from electrode/electrolyte side reactions taking place at both electrodes with a larger extent of side reaction at the graphite negative electrode. For the cells aged at 60 °C, irreversible capacity losses exceed substantially reversible ones, and if we assume that the electrode/electrolyte side reactions at both electrodes are similar to those at 45 °C, it suggests that the side reaction at the graphite electrode is more thermally activated than that at the LFP electrode [38]. The reversible capacity "gain" for the cells aged at 30 °C might simply be the result of the long current interruptions (i.e., the storage periods) over which the gain in 1 C_{nom}-capacity arising from long-time cell relaxation (dynamic effect) would be dominant over any self-discharge, likely negligible at SOC_{nom} = 30% and 65%. Under such a hypothesis, accumulation of the gain like it is done for capacity losses in Fig. 13, is meaningless.

4. Conclusion

This study presents the aging results of 27 commercial graphite/LFP cells stored under 9 different conditions of temperature (30 °C, 45 °C, and 60 °C) and nominal state of charge (SOC_{nom} 30%, 65%, and 100%). The extent of capacity loss was found to be directly related to the storage temperature. It is most prominent for the most severe aging condition (T = 60 °C and SOC_{nom} = 100%). Storage SOC also influences the capacity loss, though it is of secondary importance compared to storage temperature. Rate capability, impedance and PITT tests suggest that the loss of cyclable lithium is the main source of aging. The retention of rate capability on charge supports the absence of degradation of the LFP electrode while the improvement in rate capability upon discharge for the most severe aging conditions is consistent with the loss of cyclable lithium hypothesis. EIS analysis shows a slight increase of R_t (i.e., no change in the bulk transport properties of active materials) and an increase of both R_{hf}, and R_{sc}. The extent of R_{sc} increase exceeds that of R_{hf}. The incremental capacity shows that the gradual decrease of the area of the peak at high potential (3.37 V on charge) along with the shift of the peak at 3.16 V on discharge toward higher potential are consistent with the loss of cyclable lithium because of side reactions at the anode. The differential voltage vs. capacity plot confirms this hypothesis in a more quantitative way and suggests the absence of active material losses at the negative electrode. The capacity loss of graphite/LFP cells under storage (45 °C and 60 °C) is composed of reversible and irreversible parts. This capacity loss is the result of electrode/electrolyte side reactions taking place at both electrodes with a larger extent of side reaction at the graphite negative electrode.

Acknowledgments

This work was funded by the French National Research Agency through the SIMCAL research project.

SIMCAL network partners: CEA: S. Mailley, J. Lejosne, B. Crouzevialle, IFP Energies nouvelles: J. Bernard, R. Revel, EDF: L. Jamy, EIGSI: F. Duclaud, A. Mieze, IFSTTAR: S. Pélissier, J. Peter, SAFT: S. Bourlot, LEC-UTC: C. Forgez, LMS-Imagine: J. Hafsaoui, LRCS: M. Morcrette, C. Delacourt, M. Kassem, MTA Platform: C. Adès, PSA: Peugeot Citroën: D. Porcellato, M. Capelle, T. Prenant, S. Joly, VALEO: M. Ouattara-Brigaudet, D. Benchetrite.

References

[1] B. Johnson, R.E. White, J. Power Sources 70 (1998) 48.
[2] P. Arora, R.E. White, M. Doyle, J. Electrochem. Soc. 145 (1998) 364.
[3] R. Fong, U. Von Sacken, J.R. Dahn, J. Electrochem. Soc. 137 (1990) 2009.
[4] D. Zhang, B.S. Haran, A. Durairajan, R.E. White, Y. Podrazhansky, B.N. Popov, J. Power Sources 91 (2000) 122.
[5] P. Ramadass, A. Durairajan, B.S. Haran, R.E. White, B.N. Popov, J. Electrochem. Soc. 149 (2001) A54.
[6] J. Christensen, J. Newman, J. Electrochem. Soc. 152 (4) (2005) A818–A829.
[7] M. Broussely, P. Biensan, F. Bonhomme, P. Blanchard, S. Herreyre, K. Nechev, R.J. Staniewicz, J. Power Sources 90–96 (2005) 146.
[8] R.J. Gummow, A. de Kock, M.M. Thackeray, Solid State Ionics 69 (1994) 59.
[9] J.M. Tarascon, W.R. McKinnon, F. Coowar, T.N. Bowmer, G. Amatucci, D. Guyomard, J. Electrochem. Soc. 141 (1994) 1421.
[10] E. Peled, Proc. Electrochem. Soc. 94–28 (1995) 1.
[11] E. Peled, in: J.P. Gabano (Ed.), Lithium Batteries, Academic Press, New York, 1983.
[12] M. Broussely, S. Herreyre, P. Biensan, P. Kasztejna, K. Nechev, R.J. Staniewicz, J. Power Sources 97–98 (2001) 13.
[13] K. Ammine, C.H. Chen, J. Liu, M. Hammond, A. Jansen, D. Dees, I. Bloom, D. Vissers, G. Henriksen, J. Power Sources 97–98 (2001) 684.
[14] I. Bloom, B.W. Cole, J.J. Sohn, S.A. Jones, E.G. Polzin, V.S. Battaglia, G.L. Henriksen, C. Motloch, R. Richardson, T. Unkelhaeuser, D. Ingersoll, H.L. Case, J. Power Sources 101 (2001) 238.
[15] D. Aurbach, B. Markovsky, A. Rodkin, M. Cojocaru, E. Levi, H.J. Kim, Electrochim. Acta 47 (2002) 1899.
[16] R.B. Wright, C.G. Motloch, J.R. Belt, J.P. Christophersen, C.D. Ho, R.A. Richardson, I. Bloom, S.A. Jones, V.S. Battaglia, G.L. Henriksen, T. Unkelhaeuser, D. Ingersoll, H.L. Case, S.A. Rogers, R.A. Sutula, J. Power Sources 110 (2002) 445.
[17] D.P. Abraham, J. Liu, C.H. Chen, Y.E. Hyung, M. Stoll, N. Elsen, S. Maclaren, R. Twesten, R. Haasch, E. Sammann, I. Petrov, K. Amine, G. Henriksen, J. Power Sources 119–121 (2003) 511.
[18] R.G. Jungst, G. Nagasubramanian, H.L. Case, B.Y. Liaw, A. Urbina, T.L. Paez, D.H. Doughty, J. Power Sources 119–121 (2003) 870.
[19] K. Asakura, M. Shimomura, T. Shodai, J. Power Sources 119–121 (2003) 902.
[20] B. Markovsky, Y. Talyossef, G. Salitra, D. Aurbach, H.J. Kim, S. Choi, Electrochem. Commun. 6 (2004) 821.
[21] R.P. Ramasamy, J.W. Lee, B.N. Popov, J. Power Sources 166 (2007) 266.
[22] Q. Zhang, R.E. White, J. Power Sources 179 (2008) 793.
[23] A.K. Padhi, K.S. Nanjundaswamy, J.B. Goodenough, J. Electrochem. Soc. 144 (1997) 1188.
[24] A.K. Padhi, K.S. Nanjundaswany, C. Masquelier, S. Okada, J.B. Goodenough, J. Electrochem. Soc. 144 (1997) 1609.
[25] D.K. Kim, J. Kim, Electrochem. Solid State Lett. 9 (2006) A439.
[26] K. Striebel, A. Guerfi, J. Shim, M. Armand, M. Gauthier, K. Zaghib, J. Power Sources 119–121 (2003) 951.

[27] J. Shim, K.A. Striebel, J. Power Sources 119–121 (2003) 955.
[28] K. Zaghib, K. Striebel, A. Guerfi, J. Shim, M. Armand, M. Gauthier, Electrochim. Acta 50 (2–3) (2004) 263.
[29] M. Dubarry, B.Y. Liaw, J. Power Sources 194 (1) (2009) 541.
[30] K. Amine, J. Liu, I. Belharouak, Electrochem. Commun. 7 (2005) 669.
[31] M. Koltypin, D. Aurbach, L. Nazar, B. Ellis, Electrochem. Solid State Lett. 10 (2) (2007) A40.
[32] M. Koltypin, D. Aurbach, L. Nazar, B. Ellis, J. Power Sources 174 (2) (2007) 1241.
[33] P. Liu, J. Wang, J. Hicks-Garner, E. Sherman, S. Soukiazian, M. Verbrugge, H. Tataria, J. Musser, P. Finamore, J. Electrochem. Soc. 157 (2010) A499.
[34] J. Wang, P. Liu, J. Hicks-Garner, E. Sherman, S. Soukiazian, M. Verbrugge, H. Tataria, J. Musser, P. Finamore, J. Power Sources 196 (2011) 3942.
[35] M. Dubarry, B.Y. Liaw, M.-S. Chen, S.S. Chyan, K.C. Han, W.T. Sie, S.H. Wu, J. Power Sources 196 (2011) 3420.
[36] S.B. Peterson, J. Apt, J.F. Whitacre, J. Power Sources 195 (2010) 2385.
[37] M. Safari, C. Delacourt, J. Electrochem. Soc. 158 (10) (2011) A1123.
[38] M. Safari, C. Delacourt, J. Electrochem. Soc. 158 (12) (2011) A1436.
[39] http://www.lifebatt.co.uk.
[40] M. Kassem, C. Delacourt, unpublished results (in preparation).
[41] M. Kerlau, M. Marcinek, V. Srinivasan, R.M. Kostecki, Electrochim. Acta 52 (2007) 5422.
[42] I. Bloom, A.N. Jansen, D.P. Abraham, J. Knuth, S.A. Jones, V.S. Battaglia, G.L. Henriksen, J. Power Sources 139 (1–2) (2005) 295.
[43] I. Bloom, J. Christophersen, K. Gering, J. Power Sources 139 (1–2) (2005) 304.
[44] M. Dubarry, V. Svoboda, R. Hwu, B.Y. Liaw, Electrochem. Solid State Lett. 9 (10) (2006) A454.
[45] R. Spotnitz, J. Power Sources 113 (1) (2003) 72.
[46] Y. Ozawa, R. Yazami, B. Fultz, J. Power Sources 119–121 (2003) 918.
[47] S.E. Sloop, J.B. Kerr, K. Kinoshita, J. Power Sources 119–121 (2003) 330.